ELSEVIER

Contents lists available at ScienceDirect

Materials Characterization

journal homepage: www.elsevier.com/locate/matchar





Experimental investigation of in-situ microstructural transformations in wire arc additively manufactured maraging 250-grade steel

Yao Xu, Brajendra Mishra, Sneha P. Narra ^{1,*}

Mechanical & Materials Engineering, Worcester Polytechnic Institute, 100 Institute Road, Worcester, MA 01609, United States of America

ARTICLE INFO

Keywords: Wire arc additive manufacturing (WAAM) Maraging steel 250 Prior austenite grain refinement Precipitation hardening Anisotropy

ABSTRACT

Wire arc additive manufacturing (WAAM) is suitable for near-net-shaped manufacturing of large-scale components due to compelling factors such as high deposition rates and low feedstock costs. These factors notwith-standing, an understanding of the process-structure-property relations is necessary for the industrial use of this manufacturing process. However, the thermal cycles and heat accumulation in the WAAM process can result in different microstructural transformations. These complexities make it non-trivial to establish the process-structure-property relations. Hence, the objective of this work is to understand the various aspects of microstructure evolution in an as-fabricated material. A suite of characterization techniques, including optical microscopy, scanning electron microscopy, and electron backscatter diffraction were utilized to characterize a wire arc additively manufactured maraging steel 250 thin wall. The characterization findings show grain refinement and variation in precipitation categories and volumetric fraction as a function of the height of the thin wall. These variations are then qualitatively related to the thermal conditions during fabrication. Overall, findings from this work shed light on the impact of thermal cycles and heat accumulation on the microstructure evolution in as-fabricated maraging steel 250.

1. Introduction

Wire arc additive manufacturing (WAAM), with its high deposition rate and low feedstock costs, is an attractive option as it allows fabrication of large three-dimensional (3D) parts within shorter lead times and at a lower cost [1,2]. However, high energy input (on the order of 1000 W) and low travel speeds (on the order of 10 mm/s) results in heat accumulation in the part with limited heat dissipation paths, thus increasing the difficulty in fabricating components with a uniform microstructure. For instance, heat accumulation was reported in prior works as well [3-6]. In addition, the repeated thermal cycles and spatially distributed temperature field in the heating and cooling conditions only add to the complexity of predicting the microstructure evolution in a wire arc additively manufactured part [7–13] Thus, the mechanical properties of fusion-based additively manufactured parts are dependent on the microstructure evolution during solidification [14-16]. Also, the thermal cycles and heat accumulation ages and tempers the material in-situ during the deposition process impacting the mechanical properties of the as-fabricated part [17,18].

Maraging steel is one of the martensitic steels with an ultra-high strength of up to 2.8 GPa [19] and a relatively good fracture toughness achieved via age hardening and the formation of retained austenite (RA) [20]. It has been widely used as a critical structural material in aerospace and military applications [21,22]. Compared to other martensitic steels, maraging steels with low-carbon concentration gain strength from the dislocation accumulation at the submicron-scaled lath martensitic structure [23,24]. In addition, the main strength contributor of maraging steel is their well-dispersed fine intermetallic compounds such as Ni₃Mo, Ni₃Ti, and Fe₂Mo, which precipitate from the supersaturated iron-nickel lattice and grow during aging heat treatment [25,26]. Similar observations were reported in additively manufactured maraging steel for both laser based methods and wire arc methods [27,28].

Prior literature on additively manufactured maraging steel features utilization of both laser powder bed fusion (L-PBF) additive manufacturing (AM) and WAAM processes. However, it is heavily skewed towards L-PBF process, with information on process optimization [29–32], microstructure evolution [27,33–36], and post heat treatment [37,38]. Limited information is available on maraging steel

^{*} Corresponding author.

E-mail address: snarra@andrew.cmu.edu (S.P. Narra).

¹ Current affiliation: Mechanical Engineering, Carnegie Mellon University, 5000 Forbes Avenue, Pittsburgh, PA 15213, United States of America

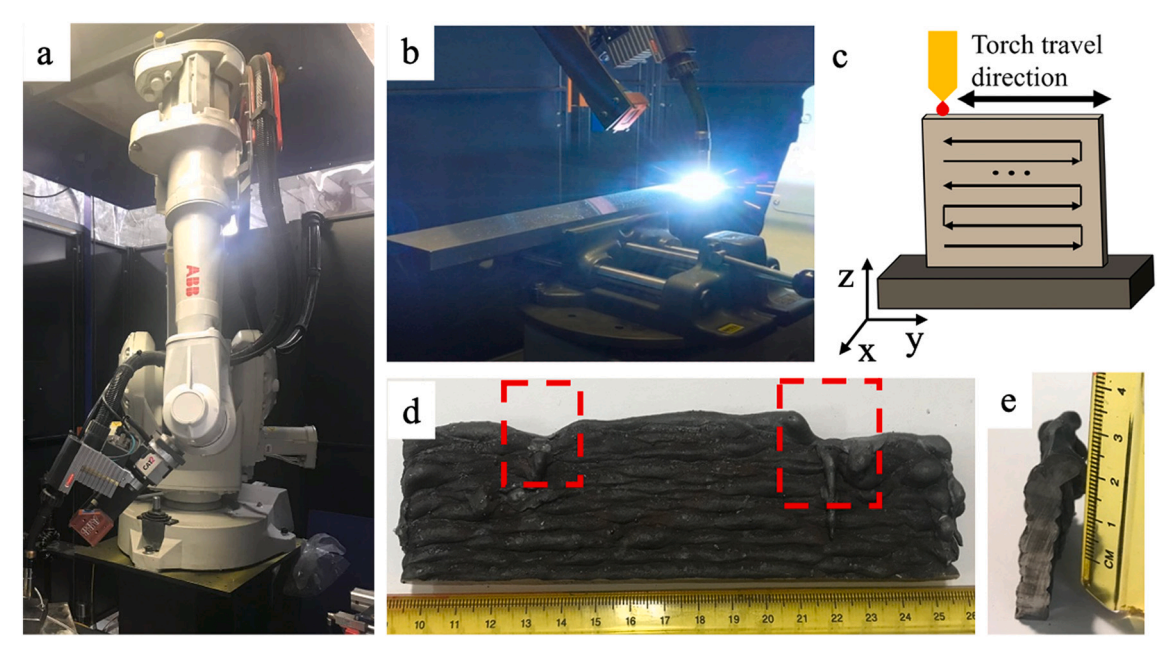


Fig. 1. (a) ABB six-axis robot arm, a Fronius wire feeder, and welding torch in the CMT- WAAM system used in this work; (b) Photograph showing the deposition of thin wall on the start plate; (c) Schematic of snake-like deposition strategy used in the thin wall sample of interest in this work, Z direction marks the deposition direction; Photographs showing the (d) front view; and (e) longitudinal section view of the as-deposited thin wall, examples of overflow defects are highlighted in red boxes. (For interpretation of the references to colour in this figure legend, the reader is referred to the web version of this article.)

fabricated using the WAAM process [28,39-42]. Due to the relatively high input power (on the order of kW) and lower travel velocity (typically on the order of 10 mm/s), high heat accumulation is observed promoting solid-state transformations during layer-by-layer deposition [6,43], high heat accumulation promotes solid-state transformations during layer-by-layer deposition [4,18]. It has been reported that the hardness of maraging steel thin wall fabricated using WAAM, increased by 20% from top to bottom region which is attributed to the aging effect due to heat accumulation during deposition [28]. Hence, this heat accumulation can count as an in-situ heat treatment step. In addition, strong partitioning was observed for major alloy element such as Ni, Mo, and Ti in the as deposited parts [27,30]. This could be due to the high cooling rates (on the order of 10^4 K/s) during deposition [41]. Moreover, the micro-segregated elements stabilize the retained austenite [42] by increasing the martensite start temperature (M_s) [44]. Thus, a fine retained austenite (RA) phase emerges in between dendritic arms, which lowers the hardness but enhances the overall toughness and ductility of the material [45,46].

In view of the complexity of the microstructural evolution of maraging steels, there is no existing work to decouple the possible strengthening (in-situ aging and grain refinement) mechanisms in the WAAM process and their effects on mechanical properties. To address this gap, this work performed a comprehensive characterization of an asfabricated maraging steel 250 thin wall deposited using cold-metal transfer (CMT)-based WAAM process. The results provide insights into the variation of hardness, grain refinement, precipitation, and presence of tempered martensite as a function of the height of the thin wall. These variations are then qualitatively related to the thermal conditions during fabrication.

2. Experimental procedures

2.1. Wire arc additive manufacturing

A cold metal transfer (CMT) WAAM system was used for the fabrication task in the current work. As shown in Fig. 1(a) and (b) this system consists of a CMT torch (Fronius, VR7000) mounted to the end of a six-axis ABB industrial robot arm, an external wire feeder from Fronius, and

Table 1Nominal composition of the wire and the start plate.

Element	Wire (TURBALOY 250*)		Start plate (annealed maraging 250 **)	
	Composition	±	Composition	±
	(wt%)	(wt%)	(wt%)	(wt%)
Ni	18.0	1.00	18.50	0.50
Co	8.0	0.50	7.50	0.50
Mo	4.9	0.30	4.80	0.20
Ti	0.40	0.10	0.4	0.10
Al	0.10	0.05	0.1	0.05
C	< 0.03	_	< 0.03	_
О	-	0.0025	-	-

From data sheet provided by *United States Welding Corporation and **Service Steel Aerospace.

Table 2Thin wall deposition parameters.

Parameter	Magnitude
Wire feed speed (WFS)	120.65 mm/s
Torch travel speed (TS)	8.47 mm/s
Arc voltage	15.6 V
Arc current	200 A
Torch angle	90°
Contact-tip-to-work distance (CTWD)	12 mm

a vise to clamp the build plate, also known as a start plate, in AM processes. The feedstock wire is a Turbaloy 250, sold by the United States Welding Corporation. This wire has a diameter of 1.2 mm and was cleaned with acetone prior to part deposition. The start plate is a 4.2 cm thick annealed maraging steel 250 substrate with dimensions of 64 cm in length and 11 cm in width and it was clamped by a vise to the worktable. Table 1 shows the nominal composition of the wire and the start plate. The CMT torch follows a pre-programmed scanning strategy, shown in Fig. 1(c). Microhardness measurements and microstructure characterization were performed on the as-fabricated thin wall.

The thin wall under consideration is 160 mm in length, 5 mm in

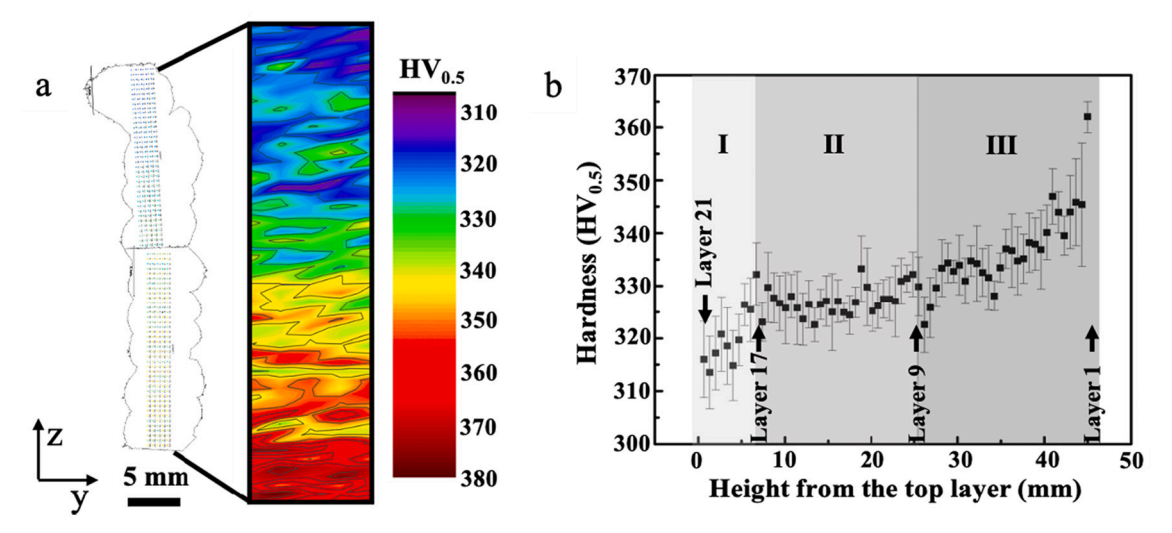


Fig. 2. (a) Illustration of the indent positions on the longitudinal section of the wall and its corresponding hardness map. The build direction is along the *Z*-axis; (b) Plot showing a three-stage increase in hardness as a function of the distance from the top surface of the thin wall. The Y error bars are one standard deviation from the mean value.

width, and consisted of 21 layers, resulting in a height of 46 mm. Table 2 lists the deposition parameters. To minimize heat accumulation, the interlayer dwell time was set to 120 s. The contact-tip-to-work distance (CTWD) was initially set to 12 mm with a 10 mm wire stick-out length. In this WAAM system, the wire stick-out length changes according to the surface topography of the previously deposited weld track to maintain a constant voltage. This changes the CTWD during the deposition process. The shield gas consisted of $16\%\ CO_2$ and 84% argon and the gas pressure was set to $410\ kPa$ during the deposition process.

2.2. Microstructure characterization and testing

The as-fabricated thin wall was separated from the substrate using a wire electrical discharge machining (EDM) method. Then, thin strips were cut at the center of the wall using a precision saw, assuming the weld track geometry reached a steady state at this location. Furthermore, these strips were divided into smaller portions to facilitate sample preparation and microstructure characterization. Following the coarse grinding and fine polishing steps, the samples used for EBSD characterization were polished using a 0.02-µm silica colloidal solution in a vibratory polisher machine. After polishing, samples were sonicated in ethanol to remove any remnants. The samples were then etched using two types of etchants. 17% Nital was used to observe solidification structure, and a combination of saturated picric acid and 0.2% hydrochloric acid were used to dye the RA phase. Metallography and crystallographic texture analysis and microhardness measurements were conducted to understand the mechanisms governing in-situ microstructural transformations during layer-by-layer deposition of a Maraging 250 thin wall.

A metallographic analysis was performed using a Nikon Epiphot 200 inverted metallurgical microscope, a Sensofar S Neox 3D optical profilometer, and a JEOL 7000F scanning electron microscope (SEM) equipped with both energy-dispersive spectrometry (EDS) and electron backscatter diffraction (EBSD) pattern detectors. The EDS spectrum was analyzed with Aztec software and the EBSD data was processed using MTEX software [47].

The microhardness measurements were performed using a Wilson VH3300 Vickers-Knoop Hardness Tester equipped with a Vickers Pyramid tip. The manufacturer suggested maximum load of 0.5 kg and a holding time of 10 s for steel parts with hardness around 300 HV. Indents were made along the wall height, using the suggested maximum load, and holding time. As shown in Fig. 2(b), five indents were made at

different heights along the deposition direction to quantify the variability in hardness measurements by error bars.

3. Results

3.1. Part quality

This section provides a qualitative description of surface roughness of the thin wall shown in Fig. 1(c). In this work, Layer 1 refers to the bottom layer and Layer 21 refers to the top layer. From visual inspection, it is evident that the two edges of the thin wall demonstrate a lower height than the center region, which can be attributed to the accumulation of start-of-the-track and end-of-the-track defects [48]. Although, an alternating scan strategy was adopted to minimize these defects, the two edges still demonstrated lower dimensions, as compared to the center indicating that the snake-like deposition strategy is not sufficient to fully compensate the deficiency. In addition, a couple of overflow defects were also observed. These defects are highlighted using a red box in Fig. 1(d). It is interesting to note that the overflow defects seem to occur at transition between the edge and the center region and appear only in the top layers of the thin wall. This could be due to the heat accumulation during layer-by-layer fabrication, which in turn, raises the deposition temperature. The heat accumulation increases the weld pool size and also results in lower cooling rates, thus promoting the possibility of weld overflow [4,49,50]. Fig. 1(e) shows the cross-section of the center region of the as-fabricated thin wall. The bottom region of the part has a better printing accuracy, while the top region is more likely to show off-center deposition due to instability of the weld pool [51]. In summary, both weld pool-scale and part-scale phenomena govern the part quality.

3.2. Microhardness

An average of 23% increase in hardness was observed from the top of the wall to the bottom, as shown in Fig. 2(a). This increase in hardness from the top to the bottom of the wall indicates that the layer-by-layer fabrication-induced microstructural transformations driven by repeated thermal cycles and heat accumulation that could result in insitu strengthening. The deposition of new layers can result in an increase in the temperature of the previous layers due to heat propagation towards the substrate via conduction. This emulates a transient in-situ heat treatment that could significantly increase the hardness from

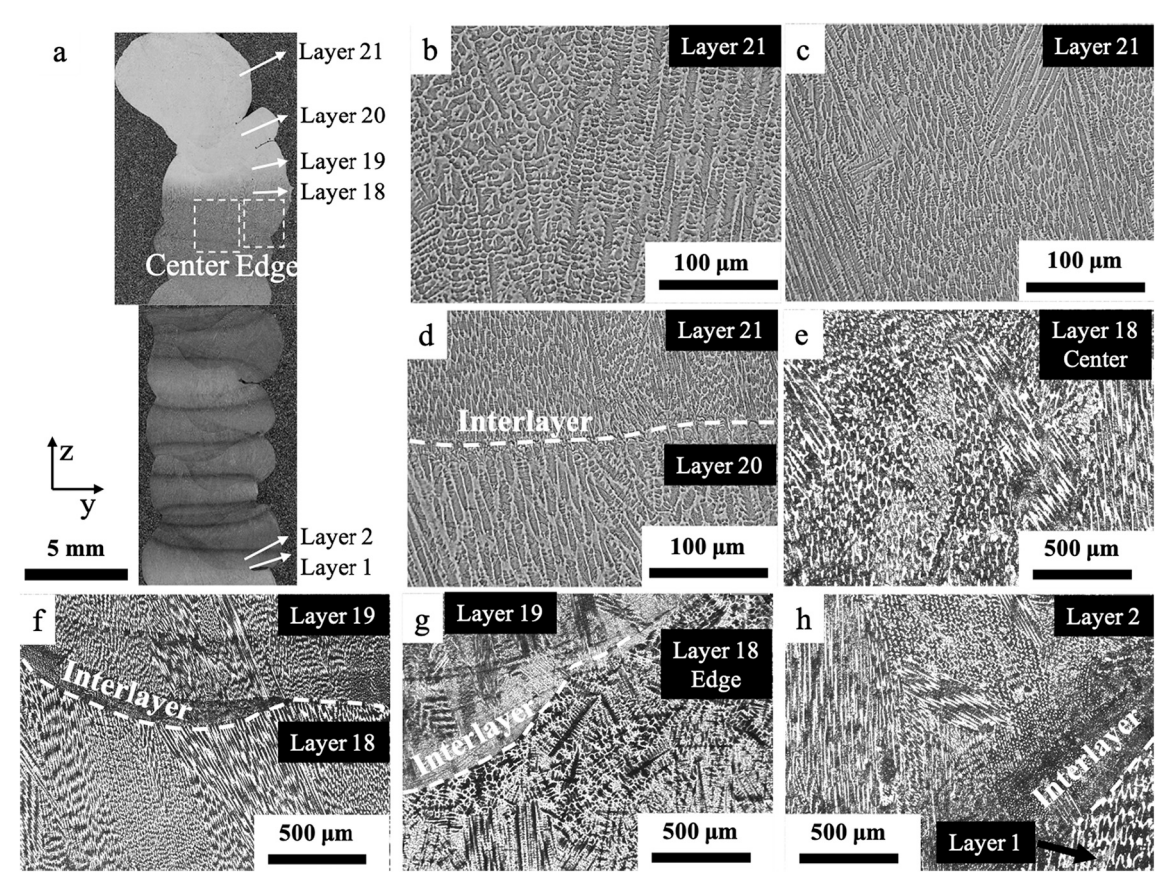


Fig. 3. (a) Low magnification optical micrograph showing the overall contrast along the wall height resulting from varied microstructure; high magnification micrograph of the solidification substructure in the (b) top region of the weld bead in Layer 21, (c) center region of the weld bead in Layer 21, and (d) interface between Layer 20 and Layer 21; (e) Relatively darker contrast in the micrograph taken from the center region of the weld bead microstructure indicating tempering in Layer 18; Tempered martensite observed in Layer 18, Layer 19, and at the interface (f) near the center region and (g) near the edge region of the weld bead; (h) Tempered martensite observed near the bead and interface region in Layer 1 and Layer 2.

310 HV to around 330 HV, as shown in Region I in Fig. 2(a). Then, the variation of hardness becomes less pronounced in Region II. On the other hand, as the deposition continues, the microhardness further increases up to 360 HV in Region III. This indicates a possible occurrence of another strengthening mechanism that may contribute to an increase in the hardness in the bottom region (Region III) of the thin wall. Hence, it is important to understand the in-situ microstructural transformations to explain the non-uniform variation in hardness along the wall height, which is the focus of this work.

3.3. Microstructure characterization

$3.3.1. \ \ Solidification \ microstructure$

This discussion focuses on the solidification substructure/pattern formed at solidification and the martensitic structure that can undergo tempering due to thermal cycles in the layer-by-layer fabrication. Fig. 3 (a) shows a high-level overview of the cross-sectional microstructure of the as-fabricated maraging 250 steel wall at different layers. Clear layered structure can be observed. The top layer formed a large round cross-section which is different from the lower layers, which can be owing to that the newly deposited layer becomes unstable and at the risk to overflow from the previous layers due to the heat accumulation. The relatively darker contrast is due to the lath martensite microstructure observed in these regions under same etching and imaging conditions. Fig. 3(b–d) illustrates dendritic solidification bands in Layers 21 and 20, located in the top region of the thin wall. The microstructure from the top surface of Layer 21 changes from columnar dendrites in Fig. 3(b) to a coarse cellular structure in Fig. 3(c), and to a fine cellular structure in

Fig. 3(d), which indicates that the cooling rate was reduced during solidification of the new bead [52]. On the other hand, Fig. 3(e-h) shows the microstructure in the subsequent layers of the thin wall. This microstructure represents traditional lath martensitic bands unlike the solidification structure observed in Layers 20 and 21. It indicates that the top two layers maintain the microstructure formed at solidification without any in-situ heat treatment, whereas the martensite in the bottom layers experience tempering due to repeated thermal cycles and the heat accumulation. Additional observations in Fig. 3(f)-(h) show an abrupt change in lath martensite band size between two neighboring layers. This indicates that these remelted regions that originally comprise the microstructure in Fig. 3(d) undergo tempering as they transform to their current form. Additionally, the center region and the edge region of the thin wall identified in Fig. 3(a) consist of different microstructure at the same height. For instance, Fig. 3(e) illustrates lath martensitic band structure in the center region of Layer 18, while the edge region in Fig. 3(g) shows equiaxed dendrites. Considering its proximity to the remelted region of Layer 19, the originally formed equiaxed dendritic structure at solidification in Layer 18 could undergo tempering during the deposition of Layer 19.

To summarize these findings, high magnification optical microscopy with a focus on the solidification substructure along the wall height indicates in-situ tempering that occurs during the layer-by-layer fabrication. The lath martensitic structure derives its strength from the twinning plane and the lath block boundary can effectively pin the dislocations. However, the tempering process can slightly reduce hardness and increase ductility [53].

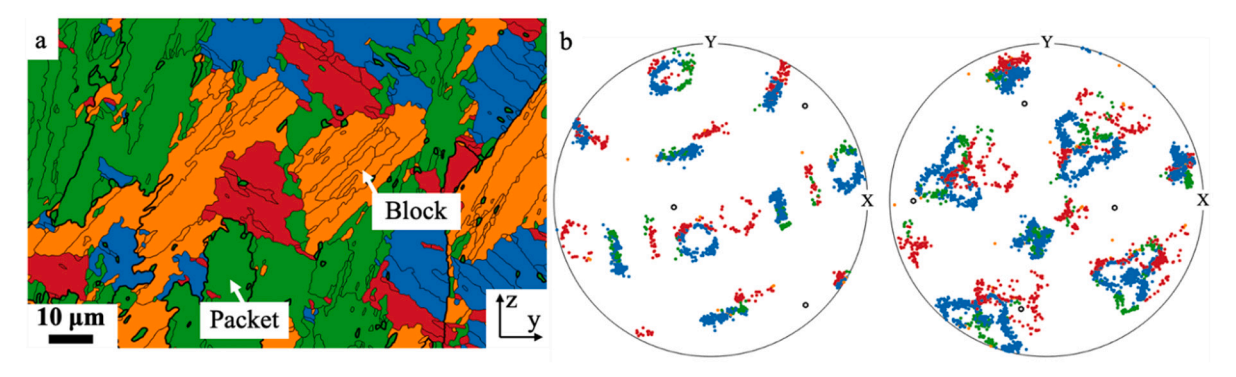


Fig. 4. (a) An example martensite variant map that shows the block and packet structure in the as-fabricated thin wall sample extracted from Layer 21; (b) (100,110) pole figures showing orientation of the martensite variants. The hollow black circles indicate the average orientation of the parent austenite phase.

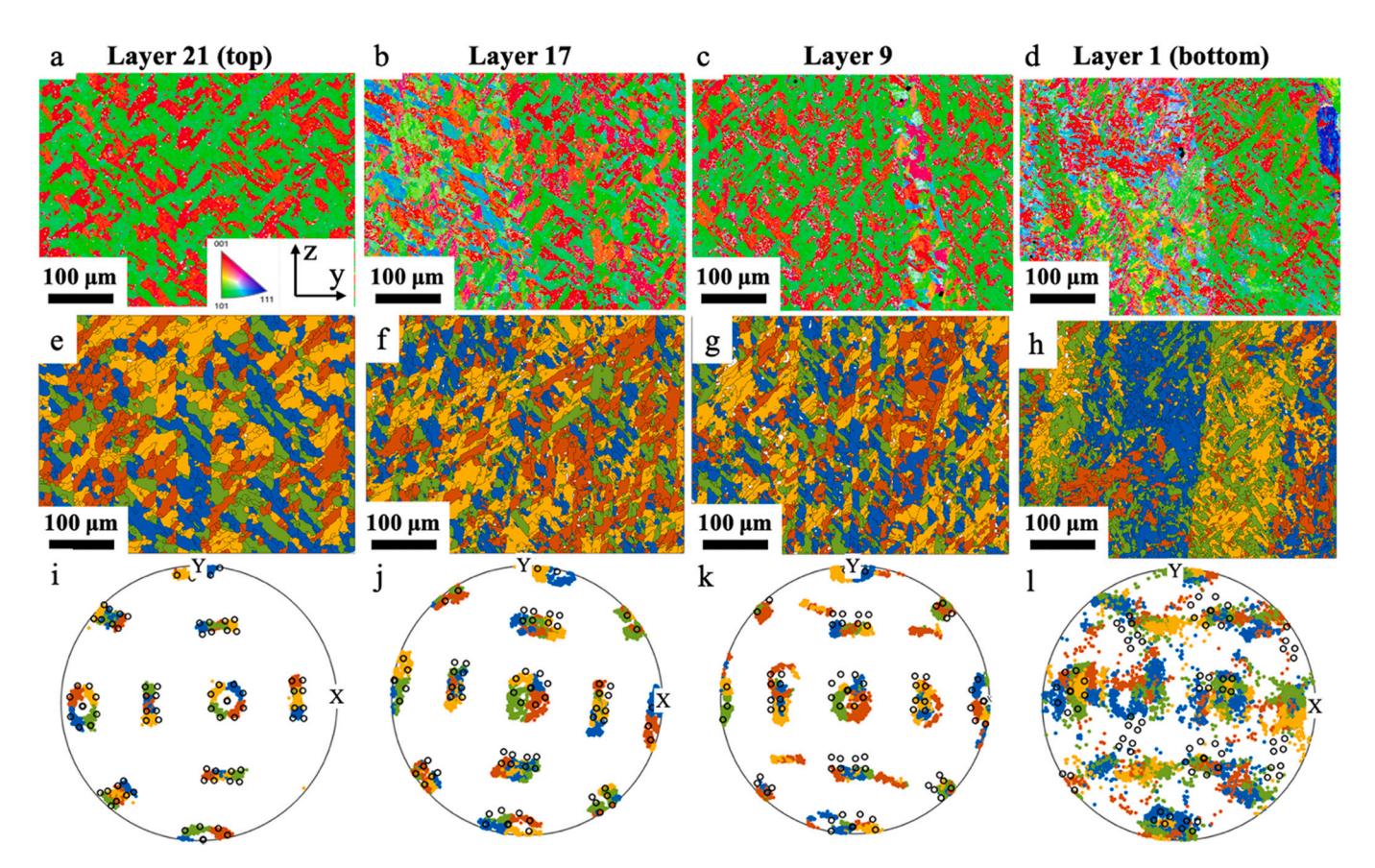


Fig. 5. (a–d) Inverse pole figures of samples extracted from Layers 21 (top), 17, 9, and 1(bottom) qualitatively, showing blocks oriented at approximately \pm 45° with the deposition direction; (e–h) Martensite variant maps of samples extracted from Layers 21, 17, 9, and 1 that correspond to the (100) pole figures in (i–l); (i–l) (100) pole figures showing a comparison between the observed martensite variant orientations and theoretical orientations shown by hollow black circles. The theoretical orientations are derived using the K-S relation with the average orientation of the RA grains as the orientation of parent phase.

3.3.2. Prior austenite grain structure

The austenite phase undergoes diffusionless phase transformation as the material cools to the M_s temperature, resulting in the formation of lath martensite. Within a PAG, the martensitic phase shows a hierarchical sub-grain structure that consists of packets, blocks, and laths [23,24]. Fig. 4(a) shows example hierarchical structure from the EBSD data analyzed in this work illustrating packets and blocks, while laths are a fundamental crystallographic unit of martensite phase and require a sub-micron scale resolution. As a result, laths are not distinguishable in Fig. 4(a).

Each set of these martensite orientations follow the Kurdjumov-Sachs (K-S) orientation relation [54] to describe the 24 unique

crystallographic lath variants that can develop from a single parent austenite grain. These laths align parallel to each other to form blocks that consist of a pair of different variants. The parallel blocks that have a common habit plane from the orientation of the parent phase arranges as packets. It is reasonable to state that the lath martensite in Fig. 4(a) is transformed from two PAGs with an orientation difference of around 30° , since the (100) and (110) pole figures in Fig. 4(b) indicate two parent-child orientation relations that are offset from each other.

Further analysis of the EBSD data collected from different wall heights show micron-scaled martensite blocks oriented at around 45° with the build direction; see Fig. 5(a)–(d). The texture of these martensite blocks qualitatively indicate that the orientation of their

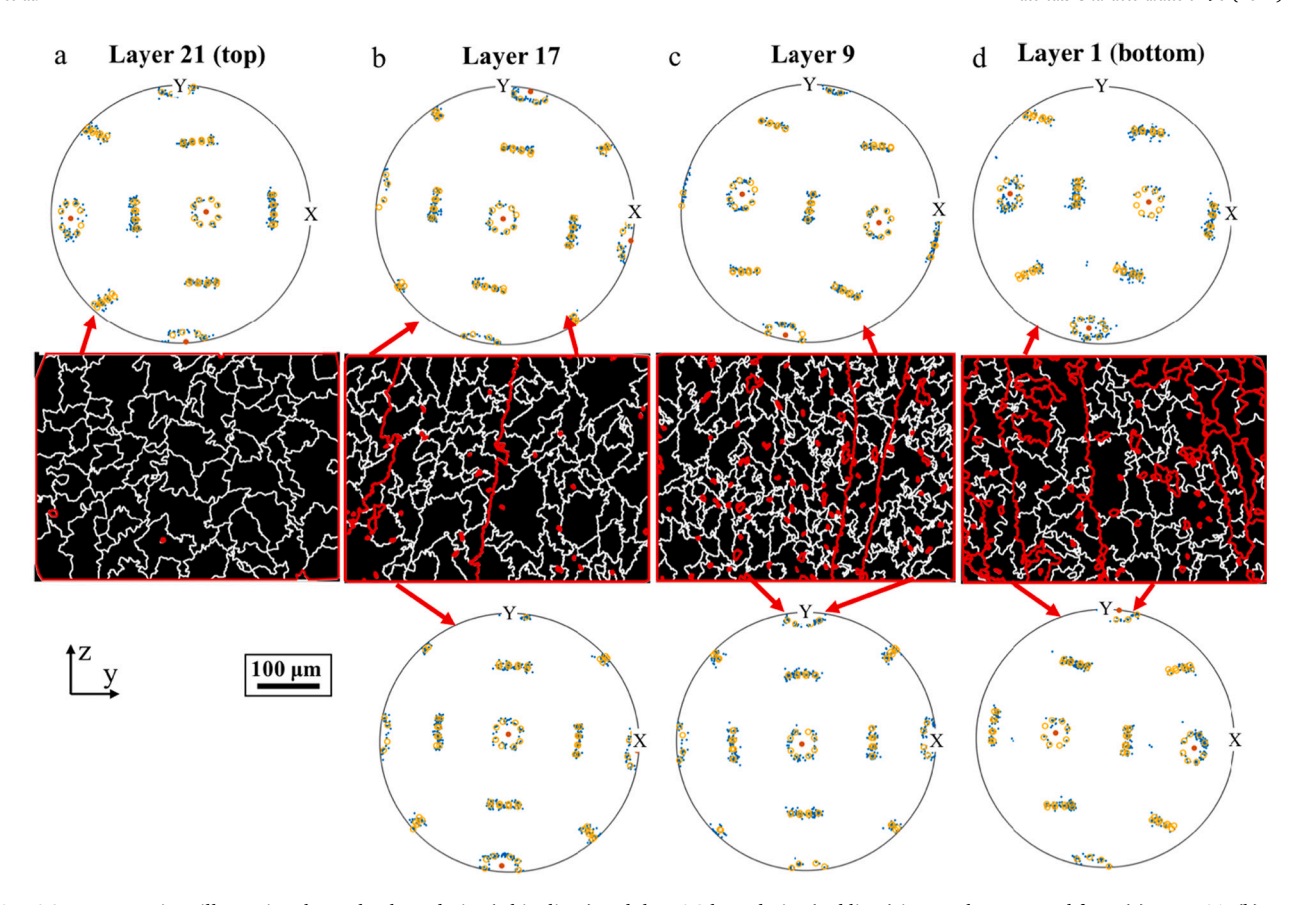


Fig. 6. PAG reconstructions illustrating the packet boundaries (white lines) and the PAG boundaries (red lines) in samples extracted from (a) Layer 21, (b) Layer 17, (c) Layer 9, and (d) Layer 1. The dispersed red regions within a PAG and along the block boundaries represent the nuclei of the reverted austenite. The (100) pole figures show a clear match between the observed martensite variant orientations (shown as blue circles) in a single PAG, and theoretical orientations (shown as hollow yellow circles) derived using the K-S relation and the orientation of the reconstructed parent phase (shown as red circles). (For interpretation of the references to colour in this figure legend, the reader is referred to the web version of this article.)

parent grains aligns with the build direction. Furthermore, the orientation of the prior austenite grains along the build direction could be due to the conduction-based heat transfer towards the substrate during the layer-by-layer fabrication process.

A qualitative description of the transformed microstructure is provided as a background to the quantitative analysis discussed in the following section. Fig. 5(e)-(h) shows martensite variants that corresponds to Fig. 5(a)-(c) after performing block coarsening by 3 µm and variant classification using optimized K-S orientation relation by averaging the orientations of the RA grains as parent phase's orientation. Fig. 5(i–l) shows the pole figures of the martensite blocks along the (100) direction. In Layer 21, the martensite variants follow the prediction of K-S relation indicating that all the martensite is transformed from one PAG and any RA in Layer 21 is directly inherent from the parent phase. On the other hand, in Layer 17, two sets of martensite parent-child orientation relations appear, and the theoretical K-S relation does not fit them accurately. This disagreement indicates that two PAGs emerge in Layer 17, and that the RA is no longer a remnant of the austenite formed during solidification, but rather is reverted from the martensite phase during the thermal cycles. Further, Fig. 5(k) indicates a similar trend occurs in Layer 9 as well. Finally, in the bottom layer, the variants relations become undistinguishable, which indicates that many finer PAGs may emerge in this layer.

Further characterization of the transformation of PAGs provides information on the mechanisms governing martensitic microstructure evolution and reverted austenite formation. The procedure for PAG reconstruction from the orientation of the child martensite variants comprises block boundary pair identification, misfit calculation with parent-child orientation relations, classification of the misfit distribution

to form packets, and combining packets that belong to one PAG [55]. The misorientations of the block boundary were identified and then compared with the parent-child orientation relations determined from the theoretical K-S relation optimized via Tuomo Nyyssönen's iteration method [56]. The packets are reconstructed by classification of the misfit between the misorientations of the block boundary and optimized K-S relations. Finally, merging packets with similar parent orientations gives the reconstructed PAGs.

Fig. 6(a)–(d) shows the packet boundaries and PAG boundaries at various locations in the wall. The resulting pole figures from the analysis show a good match for all parent-child phases. In Layer 21, all martensite blocks belong to one PAG, which agrees with Fig. 6(a). After four additional thermal cycles, the PAGs refine into two grains with similar orientation in Layer 17. In addition, an austenite phase (shown as red dots in Fig. 6(b)) is observed along the block boundaries and dispersed within a PAG. Further, reconstruction in Layer 9 shows two PAGs with different orientations. Notably, more nuclei are present in Fig. 6(c). Finally, in the bottom layer, in addition to the two PAGs with different orientations, the austenite nuclei start to coarsen, which explains the disarrayed pole shown in Fig. 5(l).

In summary, Fig. 6(a–d) demonstrates the PAG refinement that occurs during the layer-by-layer fabrication of the thin wall. The PAG refinement can lead to block size refinement [57]. This results in an increase in high-angle boundaries in martensite microstructure, which act as effective barriers to dislocation movement during the deformation of lath martensite and affect the strength and ductility of the material as per the Hall-Petch relationship [58,59]. Moreover, changes in dislocation density and carbon distribution (in solution or forming carbides) through the microstructure may occur because of PAG reduction by

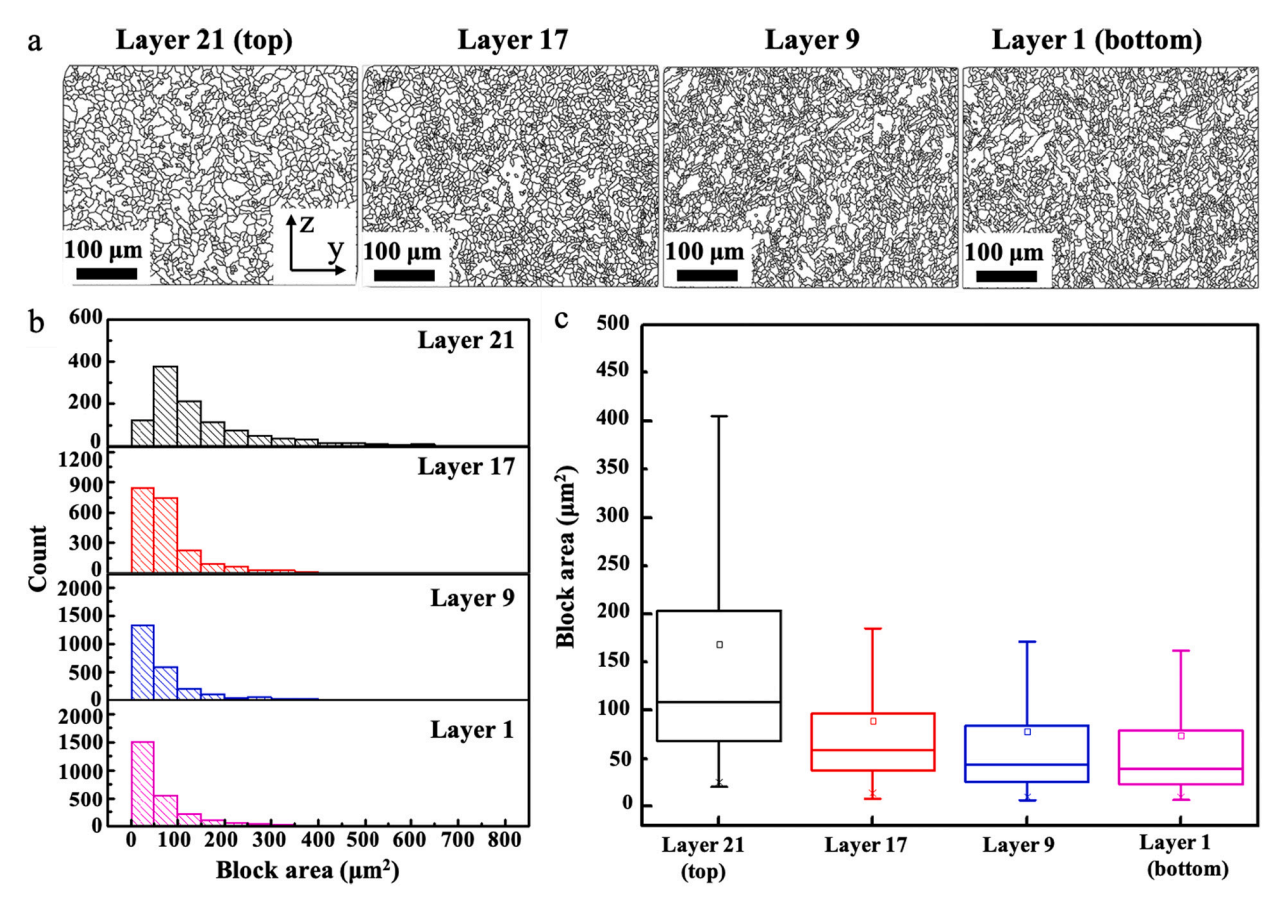


Fig. 7. (a) Illustration of the martensite blocks; (b) Histogram showing the variation in the quantity and size of the martensite blocks as a function of layer number in the thin wall; (c) Summary of the block size measurements from samples extracted from different layers. The Y error bars are one standard deviation from the mean value

thermal cycling, which increases measured hardness [60].

3.3.3. Martensite block structure

To facilitate martensite block identification, the clean-up steps comprise eliminating precipitation phases, grain coarsening (area larger than 6 μm^2), and identifying block boundaries (misorientation that exceeds 3^o). Fig. 7(a) demonstrates martensite block boundaries and Fig. 7 (b) shows the martensite block size distribution at various locations along the wall height. From Layer 21 (top layer) to Layer 1 (bottom layer), more fine martensite blocks emerge. This observation corresponds to the nucleation process that occurs during PAG refinement. As shown in Fig. 7(c), the average size of the blocks reduces from 168 μm to 80 μm within the first 4 thermal cycles and then reaches a steady state, where the size reduction is at a lower rate from Layer 17 to Layer 1. The resulting increase in strength can be estimated using the Hall-Petch relationship shown in Eq. 1

$$\sigma_{g} = k/\sqrt{D} \tag{1}$$

where, σ_g is the strength gain by the Hall-Petch effect and k is the microstructure-dependent constant. The strength will increase by 30% as the block size is reduced by 53% from Layer 21 to Layer 17, which is more pronounced than the hardness increase observed in Region I in Fig. 2(b). The counteracting softening effects from tempering (Section 3.3.1) could possibly explain this disagreement between the expected increase in strength and the measured values. On the other hand, from Layer 9 to Layer 1, the average block size was reduced by around 10%, which corresponds to around a 5% improvement in strength. However, the hardness increases from around 330 HV to 360 HV in Region III in Fig. 2(a) and indicates the presence of an additional strengthening

mechanism, which is discussed next.

3.3.4. Precipitation

Maraging steels gain ultra-high strength following traditional heat treatment methods, such as quenching and aging, commonly at 400°C–500°C for 2–6 h [61]. Higher temperature and different aging time ranges have been tested in precipitation kinetics research and widely employed [25,26,62]. The solutionized and quenched maraging steels will also show a hardness enhancement by 10% after aging at 200°C for only 30 s [62]. This temperature and time range match with the temperature elevation in parts due to thermal cycles or heat accumulation in AM. Furthermore, precipitates were also observed in the asfabricated components in AM [27,28]. Fig. 8 provides an overview of the precipitation microstructure of the thin wall characterized in this work.

EBSD phase mapping was employed to identify the various precipitates by gridding up a 25 µm by 30 µm area with a step size of 50 nm. At each grid, the Kikuchi diffraction maps were measured and compared with predefined theoretical direction pattern for phase identification. To quantify the variability, four such probe windows were selected for the same layer height, sampling 1 million grids for that layer providing a qualitative trend in volumetric fraction change in different precipitation phases. The predefined precipitation phases were considered as Ni₃Ti, p-Ni₃Mo, μ-Fe₇Mo₆, λ-Fe₂Mo, σ-FeMo, and R-Fe₃Mo₂ reported in the literature [25-28,62,63]. Fig. 8(a) illustrates the EBSD phase mapping results and Fig. 8(b) shows the relative composition change for different precipitation phases. In these figures, Layer 21 has a higher percentage of p-Ni₃Mo precipitates on the order of microns and the p-Ni₃Mo percentage lowers towards the bottom region of the wall indicating that this phase is not thermally stable during the layer-by-layer fabrication. The contribution of micron-scale precipitates to the strength of the material

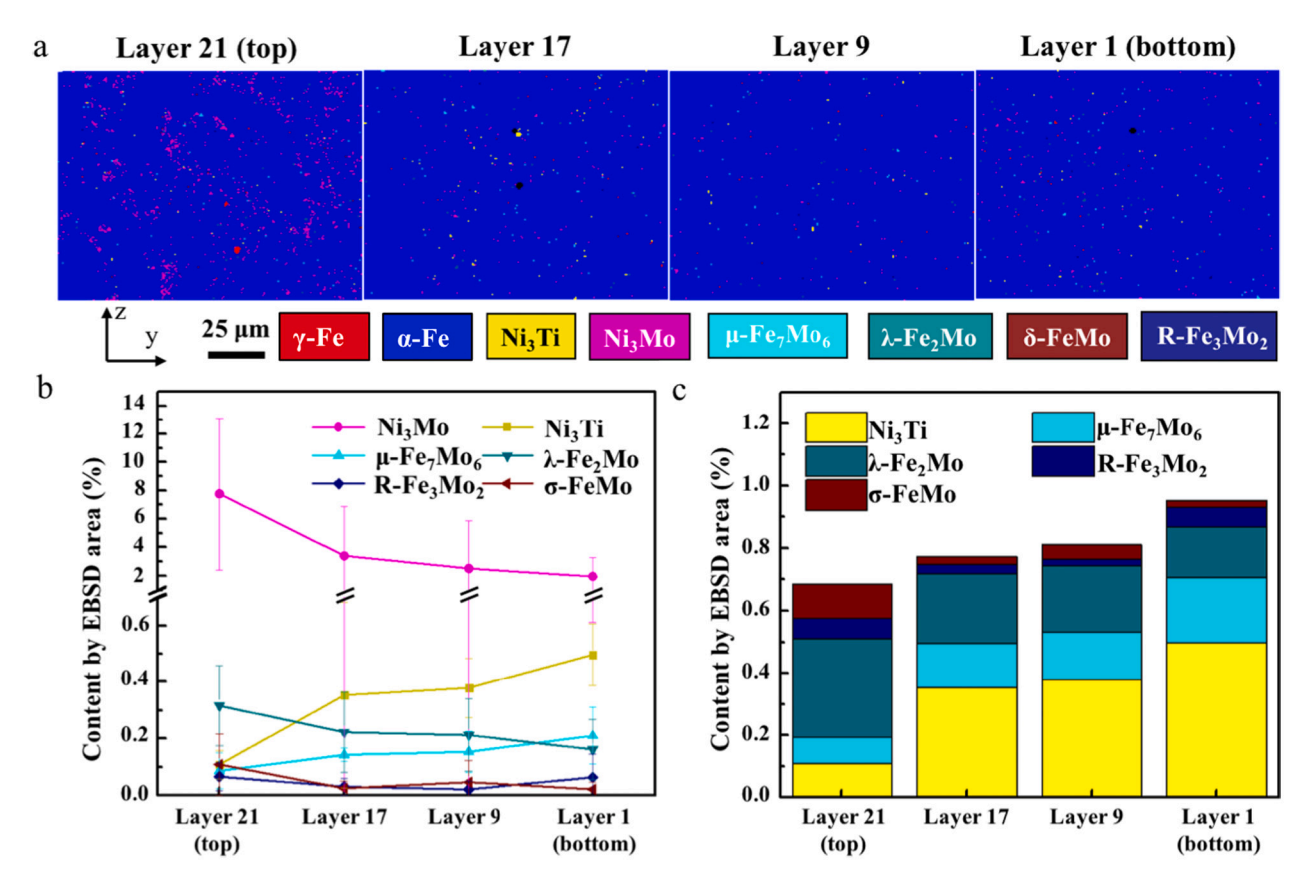


Fig. 8. (a) Qualitative demonstration of the phase distribution at different layers in the thin wall; (b) Quantitative variation in the precipitates as a function of layer number in the as-fabricated maraging steel 250 thin-wall; (c) Total amount of precipitates without considering Ni₃Mo. The Y error bars in this figure are one standard deviation on the mean value.

is less compared to the contribution of well-dispersed, nano-scale precipitations. Like the p-Ni₃Mo, the amount of λ -Fe₂Mo and σ -FeMo lowers from the top layer to the bottom layer of the thin wall. On the other hand, the percentage of Ni₃Ti and μ-Fe₇Mo₆ precipitates increase during the layer-by-layer fabrication process. Fig. 8(c) details the amount of total nano-scaled precipitates at different locations. From Layer 21 to Layer 17, the amounts of λ -Fe₂Mo, R-Fe₃Mo₂, and σ -FeMo reduce, yet Ni₃Ti and μ-Fe₇Mo₆ increase. Consequently, the total amount increased from 0.68 to 0.77 (~13%) between Layer 21 and Layer 17, which corresponds to the hardness increase in Region I in Fig. 2(a). The composition of each precipitation phase and the total amount of precipitates remain the same between Layer 17 and Layer 9, which corresponds to the steady state in Region II. Finally, because of the further increase in Ni_3Ti and μ -Fe₇Mo₆, the total precipitation amount increased by 36%, as compared to the top layer. This increase agrees with the strengthening in Region III in the hardness map. A comparison of Figs. 2(a) and 8(c) shows agreement between the trend in hardness increase and the precipitation amount.

The in-situ aging effect can be a result of two heating steps: (i) short-term aging when Ni_3Mo dissolves and Ni_3Ti and λ precipitations forms caused by thermal cycles with peak temperature ranges between $790^{\circ}C$ and $330^{\circ}C$ for a duration of 25 s per cycle when depositing a subsequent layer, as described in full detail in Section 4.2.1. This heat propagates downwards along the wall to heat the subsequent layer to an elevated temperature that can reach as high as the solutionizing temperature (around $1500^{\circ}C)$; however, this cyclic heat decays quickly as it propagates and will only be effective within several layers below the new layer, and (ii) long-term aging caused by the raised temperature (up to $330^{\circ}C)$ in the workpiece due to heat accumulation during the deposition process. It is reasonable to summarize that the short-term aging contributes to the increase in precipitation in Layer 21 to Layer 17 and the

hardening observed in Region I, whereas the diffusion-controlled precipitation mechanism during the long-term aging explains the steady state Region II and significant increase in hardness in Region III.

4. Discussion

4.1. Thermal cycles and temperature buildup in wire arc additive manufacturing

During the thin wall fabrication, the power input, depending on the arc efficiency, arc voltage, and deposition current, is around 3 kW. This energy melts the substrate and the wire, forming a weld pool and molten droplet respectively. The molten pool and the droplet solidify as the energy mainly conducts from the molten region to the previously deposited layers [64]. For a thin structure, such as the thin wall in the current work, there is limited path for heat propagation and can result in temperature build up. The layer temperature tolerance is determined by the properties of the materials and the deposition parameters such as arc length and power density [8,65]. The introduction of idle times between the deposition of subsequent layers allows the as-fabricated part to be air cooled [50]. On the other hand, the thermal cycles can span the temperature range covering an A_s temperature of 650°C or higher and the temperature as low as an M_s temperature of 160°C [8]. The broad shift in temperature range promotes a rapid transformation between austenite and martensite phases that leads to unique phenomena, such as PAG refinement and martensite reversion that can result in nucleation of RA [57]. In addition, the resulting heat accumulation can increase the temperature of the substrate and the deposited workpiece significantly. This means the part temperature is high, which reduces the heat dissipation rate, and hence, reduces the cooling rate in the newly deposited layer.

Fig. 9

$T=1500^{\circ}\mathrm{C}$	$L \rightarrow \gamma + TiC$
$T = 790^{\circ}$ C	$\lambda(Fe_2Mo)$ precipitation
$T = 550^{\circ}$ C	Ni ₃ Ti precipitation
$T = 410^{\circ}\text{C}$	$\lambda(\text{Fe}_2\text{Mo}) + \text{TiC} \rightarrow \text{Ni}_3\text{Ti} + \text{M}_6\text{C}((\text{Fe}, \text{Mo})_6\text{C})$
$T = 400^{\circ}$ C	$\gamma \rightarrow \lambda(Fe_2Mo) + \alpha$
$T = 330^{\circ}$ C	$\lambda(\text{Fe}_2\text{Mo}) \rightarrow \mu(\text{Fe}_7\text{Mo}_6)$

4.2. Strengthening mechanisms

4.2.1. Precipitation hardening

Maraging steel can be age hardened at temperatures as low as 200°C. For instance, aging for 15 to 60 s at 480°C to 500°C can enhance the hardness to 450-525 HV and aging at 200°C for time intervals as low as 30 s can improve hardness by 10% [62]. Understanding this behavior involves an investigation of thermodynamics and precipitation reactions. Fig. 9(a) shows the liquidus projection of an Fe-Ni-Mo system calculated by Thermo-Calc 2021a with TCFE11 database. The liquidus temperature and solidus temperature for maraging steel 250 is around 1500°C and 1450°C, respectively. In Fig. 9(a), this temperature range corresponds to Liquid $+ \gamma$ phase at nominal composition. However, the high cooling rate (up to 10^4 K/s [41]) of the WAAM process promotes strong element partitioning during solidification, especially for Mo [66]. At 18 wt% Ni and with Mo partitioning, the solidified phases will fall into the L + p-Ni₃Mo + R-Fe₃Mo₂ + σ -FeMo regions between freezing range of 1450°C and 1500°C. As a result, the liquid in the last stages of solidification contains a large amount of rejected Mo and it will solidify to form micron-scale p-Ni₃Mo precipitates, as shown in Fig. 8(a) and

results in a higher initial composition of R-Fe $_3$ Mo $_2$ and σ -FeMo in Layer 21. Furthermore, Fig. 9(b) illustrates the isothermal ternary phase diagram of an Fe-Ni-Mo system at 1200°C to which the previously deposited layer can be heated up by the successive layer. The p-Ni $_3$ Mo is not stable in a region with Ni <20 wt%, which indicates that the remnant p-Ni $_3$ Mo post solidification will dissolve during successive thermal cycles in the lower layers to form σ -FeMo, μ -Fe $_7$ Mo $_6$, and γ . Note that the σ -FeMo is also a non-stable phase at low temperature and further converts to other phases, thus explaining the reduction in σ -FeMo that is shown in Fig. 8(c).

Fig. 9(c) shows the phase diagram at nominal element composition of Fe-Ni-Co8-Mo5-Ti0.4-Co.02 system as a function of temperature and Ni content. Graphite phase was ruled out from calculation considering the low concentration of carbon. For a nominal Ni content (18.0 wt%), solutionizing occurs at approximately 790°C. Above this temperature, only the TiC is present in the matrix. The precipitation temperature of commonly reported intermetallic phases, such as λ -Fe₂Mo is 790°C, Ni₃Ti is 550°C, and M₆C-(Fe, Mo)₆C is 400°C. The λ -Fe₂Mo will further transform to μ -Fe₇Mo₆ at 330°C. Fig. 9(d) shows the solid-state transformations that occur during equilibrium cooling at the nominal composition stoichiometry Fe-Ni18-Co8-Mo5-Ti0.4-Co.02. This reaction sequence provided below explains the changes observed in EBSD at various locations in Fig. 8, where λ -Fe₂Mo reduces while μ -Fe₇Mo₆ and Ni₃Ti increase during the layer-by-layer deposition process.

4.2.2. Grain refinement

The thermal cycling of maraging steels leads to PAG and martensitic microstructure (blocks) refinement, which results in an increase of the

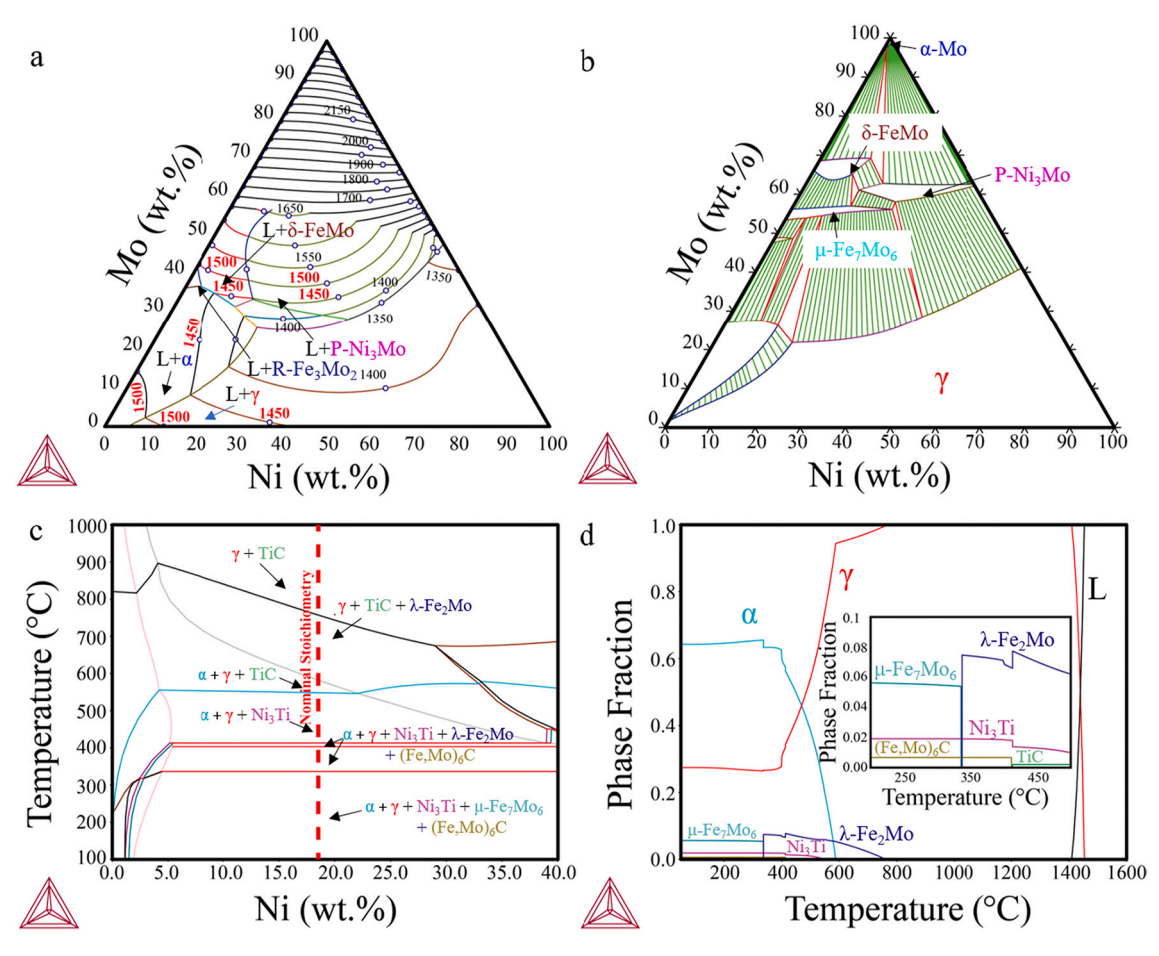


Fig. 9. (a) Ternary liquidus projection of the Fe-Ni-Mo system; (b) Isothermal ternary phase diagram at 1200°C of the Fe-Ni-Mo system; (c) Phase diagram with varying Ni composition in maraging 250 steel; (d) Phase fraction versus temperature of maraging 250 steel that highlights the solid-state transformations as a function of temperature.

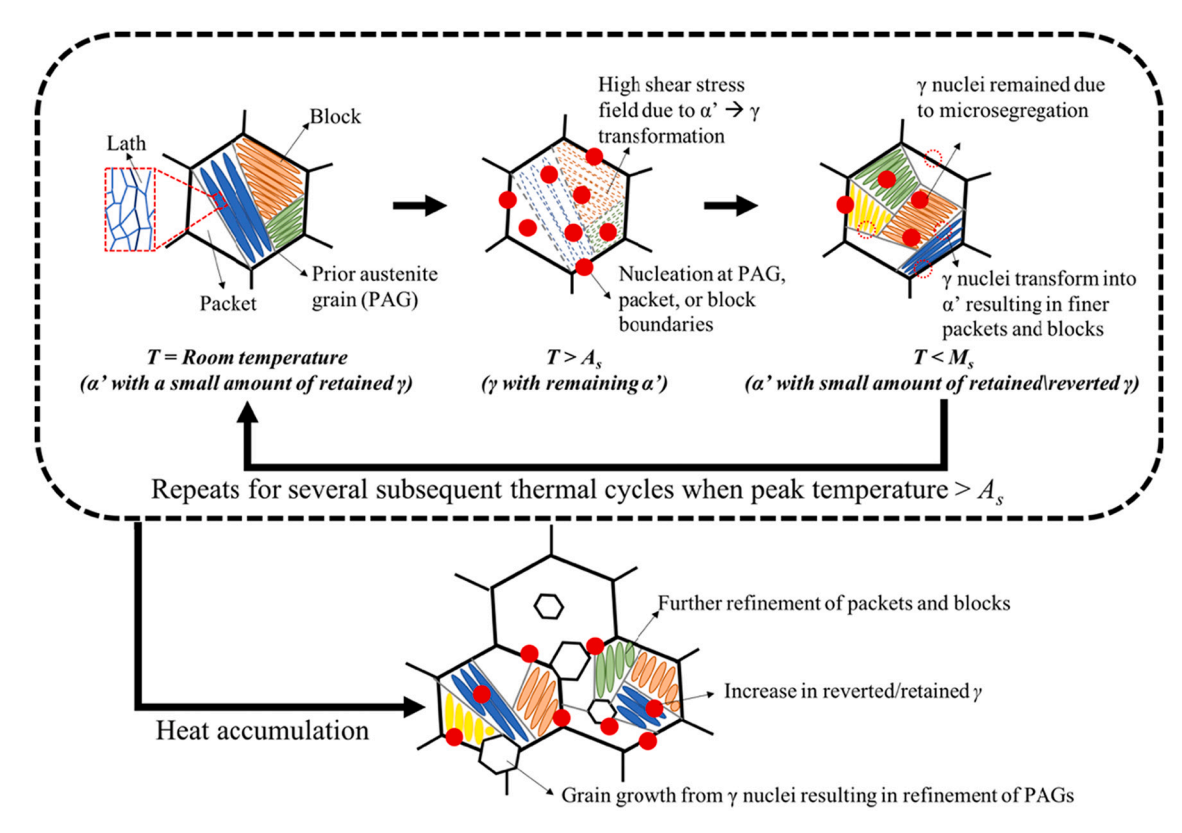


Fig. 10. Schematic illustration PAG refinement mechanisms: nucleation governed by high temperature thermal cycling and grain growth throughout the deposition affected by heat accumulation.

density of high misorientation angle boundaries [52]. Fig. 10 illustrates the mechanisms that govern PAG refinement during thermal cycles. During the thermal cycling, when the peak temperature exceeds the As temperature, the transformation from martensite to austenite produces a strong localized shear strain field among grains due to the 3-4% volume difference between the martensite and austenite crystal structures [67,68]. This localized shear strain field drives nucleation of new reverted austenite at the grain boundaries. In the lower region of the thin wall where the peak temperature of thermal cycles is not high enough to drive martensite to austenite transformation, the nucleation process ceases. However, the accumulated heat could promote the grain growth and, hence, PAG refinement. In the current work, the nucleation of the austenite phase and the growth of the nuclei was observed throughout the sub-layers. The resulting reduction in block size was found to be continuous throughout the deposition and to be more pronounced in the top region.

5. Conclusions

In the present work, a 21-layer maraging steel 250 thin wall was fabricated using a cold metal transfer-based wire arc additive manufacturing process. Overflow defects were identified in the top region of the thin wall. The hardness map of the as-fabricated thin wall component showed a three-stage hardening process: i) in Region I, the hardness increased by 10% from Layer 21 to Layer 17; ii) in Region II, the hardness remained consistent from Layer 17 to Layer 9; and iii) in Region III, the hardness increased further by 13% from Layer 9 to Layer 1. Overall, an average of 23% increase in hardness was observed along the height of the wall.

In Region I, the nucleation of the prior austenite and the martensite block size refinement was observed, which indicates that the peak temperature is higher than the A_s temperature. Meanwhile, the micronscale Ni₃Mo precipitates that formed during solidification due to strong

Mo partitioning started to dissolve into finer $\lambda\text{-Fe}_2\text{Mo}$ and Ni $_3\text{Ti}$ precipitations in this region, which indicates short-time in-situ aging effect in this region. In Region II, the thin wall was held at an elevated temperature due to heat accumulation and the accumulated heat allows the martensitic structure to be further tempered, which softened the component. These softening effects were countered by the long-time insitu aging, which resulted in the formation and growth of $\mu\text{-Fe}_7\text{Mo}_6$ and Ni $_3\text{Ti}$ precipitates. The hardness continues to increase further in Region III. This is an indication of long-time aging caused by the accumulated heat outweighing the softening mechanisms.

In summary, the thermal cycles and heat accumulation during the layer-by-layer deposition process can result in both strengthening and softening of the as fabricated maraging 250 steel. Strengthening results from PAGs/blocks refinement and/or precipitation hardening. On the other hand, martensite tempering results in softening. These competing in-situ strengthening and softening mechanisms could have caused the three-stage hardening observed in the thin wall studied in this work.

Data availability

The raw/processed data required to reproduce these findings cannot be shared at this time as the data is currently being used in another study.

Declaration of Competing Interest

The authors declare that they have no known competing financial interests or personal relationships that could have appeared to influence the work reported in this paper.

Acknowledgements

The authors acknowledge Alex Michelson at Solvus Global for

performing the experiments on their WAAM equipment. This work was enabled by the support of U.S. Army Combat Capabilities Development Command Army Research Laboratory under contract W911NF1920108, WPI faculty start-up funding, and Materials and Manufacturing Engineering Program Graduate Teaching Assistantship. We are grateful to Prof. Bryan Webler at Carnegie Mellon University for reviewing the manuscript prior to submission, and Rui Wang at WPI for fruitful discussions on thermodynamic calculations and for sharing their insights on steel microstructure. We are grateful to WPI Surface Metrology Lab that houses the Sensofar S-Neox digital microscope, which the authors used for image stitching in the current work.

References

- [1] S.W. Williams, F. Martina, A.C. Addison, J. Ding, G. Pardal, P. Colegrove, Wire + arc additive manufacturing, Mater. Sci. Technol. 32 (7) (2016) 641–647, https://doi.org/10.1179/1743284715y.0000000073.
- [2] J.L.Z. Li, M.R. Alkahari, N.A.B. Rosli, R. Hasan, M.N. Sudin, F.R. Ramli, Review of wire arc additive manufacturing for 3d metal printing, Int. J. Autom. Technol. 13 (3) (2019) 346–353, https://doi.org/10.20965/ijat.2019.p0346.
- [3] C. Xia, et al., A review on wire arc additive manufacturing: monitoring, control and a framework of automated system, J. Manuf. Syst. 57 (2020) 31–45. Elsevier B.V. Oct. 01, https://doi.org/10.1016/j.jmsy.2020.08.008.
- [4] B. Wu, et al., Effects of heat accumulation on the arc characteristics and metal transfer behavior in wire arc additive manufacturing of Ti6Al4V, J. Mater. Process. Technol. 250 (2017) 304–312. Dec. https://doi.org/10.1016/j.jmatprotec.2017.0 7.037.
- [5] E.R. Denlinger, J.C. Heigel, P. Michaleris, T.A. Palmer, Effect of inter-layer dwell time on distortion and residual stress in additive manufacturing of titanium and nickel alloys, J. Mater. Process. Technol. 215 (2015) 123–131, https://doi.org/ 10.1016/j.jmatprotec.2014.07.030.
- [6] Y. Li, C. Su, J. Zhu, Comprehensive review of wire arc additive manufacturing: hardware system, physical process, monitoring, property characterization, application and future prospects, Results Eng. 13 (September 2021) (2022) 100330, https://doi.org/10.1016/j.rineng.2021.100330.
- [7] B. Wu, Z. Pan, S. van Duin, H. Li, Thermal Behavior in Wire Arc Additive Manufacturing: Characteristics, *Effects and Control*, Springer, Singapore, 2019, https://doi.org/10.1007/978-981-13-3651-5 1.
- [8] J. Xiong, R. Li, Y. Lei, H. Chen, Heat propagation of circular thin-walled parts fabricated in additive manufacturing using gas metal arc welding, J. Mater. Process. Technol. 251 (July 2017) (2018) 12–19, https://doi.org/10.1016/j. ion.com/process/10.0007/j.
- [9] C.R. Cunningham, J.M. Flynn, A. Shokrani, V. Dhokia, S.T. Newman, Invited review article: strategies and processes for high quality wire arc additive manufacturing, Addit. Manuf. 22 (June) (2018) 672–686, https://doi.org/ 10.1016/j.addma.2018.06.020.
- [10] K. Oyama, S. Diplas, M. M'hamdi, A.E. Gunnæs, A.S. Azar, Heat source management in wire-arc additive manufacturing process for Al-mg and Al-Si alloys, Addit. Manuf. 26 (December 2018) (2019) 180–192, https://doi.org/10.1016/j. addma. 2019.01.007
- [11] T.A. Rodrigues, et al., In-situ strengthening of a high strength low alloy steel during wire and arc additive manufacturing (WAAM), Addit. Manuf. 34 (January) (2020) 101200, https://doi.org/10.1016/j.addma.2020.101200.
- [12] W.C. Ke, et al., Multi-layer deposition mechanism in ultra high-frequency pulsed wire arc additive manufacturing (WAAM) of NiTi shape memory alloys, Addit. Manuf. 50 (January 2021) (2022), https://doi.org/10.1016/j. addma.2021.102513.
- [13] T.A. Rodrigues, et al., Steel-copper functionally graded material produced by twinwire and arc additive manufacturing (T-WAAM), Mater. Des. 213 (November) (2022) 110270, https://doi.org/10.1016/j.matdes.2021.110270.
- [14] J. Gockel, L. Sheridan, S.P. Narra, N.W. Klingbeil, J. Beuth, Trends in solidification grain size and morphology for additive manufacturing of Ti-6Al-4V, JOM 69 (12) (2017) 2706–2710. Dec. https://doi.org/10.1007/s11837-017-2601-6.
- [15] S.A. David, J.M. Vitek, Correlation between solidification parameters and weld microstructures, Int. Mater. Rev. 34 (1) (1989) 213–245, https://doi.org/10.1179/ imr.1989.34.1.213.
- [16] W. Ou, T. Mukherjee, G.L. Knapp, Y. Wei, T. DebRoy, Fusion zone geometries, cooling rates and solidification parameters during wire arc additive manufacturing, Int. J. Heat Mass Transf. 127 (2018) 1084–1094, https://doi.org/10.1016/j.iiheatmasstransfer.2018.08.111.
- [17] P.C. Collins, D.A. Brice, P. Samimi, I. Ghamarian, H.L. Fraser, Microstructural control of additively manufactured metallic materials, Annu. Rev. Mater. Res. 46 (2016) 63–91, https://doi.org/10.1146/annurev-matsci-070115-031816.
- [18] X. Lu, M.V. Li, H. Yang, Simulation of precipitates evolution driven by non-isothermal cyclic thermal history during wire and arc additive manufacturing of IN718 superalloy, J. Manuf. Process. 65 (April) (2021) 258–270, https://doi.org/10.1016/j.jmapro.2021.03.032.
- [19] Y. He, K. Yang, W. Qu, F. Kong, G. Su, Strengthening and toughening of a 2800-MPa grade maraging steel, Mater. Lett. 56 (5) (2002) 763–769, https://doi.org/10.1016/S0167-577X(02)00610-9.

- [20] E.A. Jägle, P.P. Choi, J. Van Humbeeck, D. Raabe, Precipitation and austenite reversion behavior of a maraging steel produced by selective laser melting, J. Mater. Res. 29 (17) (2014) 2072–2079, https://doi.org/10.1557/jmr.2014.204.
- [21] W.P. Limited, Steels for aircraft structures, in: Introduction to Aerospace Materials, 2012, pp. 232–250, https://doi.org/10.1533/9780857095152.232.
- [22] D.P.M. da Fonseca, A.L. Melo Feitosa, L.G. de Carvalho, R.L. Plaut, A.F. Padilha, A short review on ultra-high-strength maraging steels and future perspectives, Mater. Res. 24 (1) (2021), https://doi.org/10.1590/1980-5373-MR-2020-0470.
- [23] T. Zhou, J. Faleskog, R.P. Balu, J. Odqvist, H. Yu, P. Hedström, Exploring the relationship between the microstructure and strength of fresh and tempered martensite in a maraging stainless steel Fe–15Cr–5Ni, Mater. Sci. Eng. A 745 (January) (2019) 420–428, https://doi.org/10.1016/j.msea.2018.12.126.
- [24] H. Kitahara, R. Ueji, N. Tsuji, Y. Minamino, Crystallographic features of lath martensite in low-carbon steel, Acta Mater. 54 (5) (2006) 1279–1288, https://doi. org/10.1016/j.actamat.2005.11.001.
- [25] R. Tewari, S. Mazumder, I.S. Batra, G.K. Dey, S. Banerjee, Precipitation in 18 wt% Ni maraging steel of grade 350, Acta Mater. 48 (5) (2000) 1187–1200, https://doi. org/10.1016/S1359-6454(99)00370-5.
- [26] W. Sha, A. Cerezo, G.D.W. Smith, Phase chemistry and precipitation reactions in maraging steels: Part IV. Discussion and conclusions, Metall. Trans. A. 24 (June) (1003)
- [27] C. Tan, K. Zhou, W. Ma, P. Zhang, M. Liu, T. Kuang, Microstructural evolution, nanoprecipitation behavior and mechanical properties of selective laser melted high-performance grade 300 maraging steel, Mater. Des. 134 (2017) 23–34, https://doi.org/10.1016/j.matdes.2017.08.026.
- [28] X. Xu, S. Ganguly, J. Ding, S. Guo, S. Williams, F. Martina, Microstructural evolution and mechanical properties of maraging steel produced by wire + arc additive manufacture process, Mater. Charact. 143 (2018) 152–162. Sep. https:// doi.org/10.1016/j.matchar.2017.12.002.
- [29] A.F. de Souza, K.S. Al-Rubaie, S. Marques, B. Zluhan, E.C. Santos, Effect of laser speed, layer thickness, and part position on the mechanical properties of maraging 300 parts manufactured by selective laser melting, Mater. Sci. Eng. A 767 (September) (2019) 138425, https://doi.org/10.1016/j.msea.2019.138425.
- [30] K. Kempen, E. Yasa, L. Thijs, J.P. Kruth, J. Van Humbeeck, Microstructure and mechanical properties of selective laser melted 18Ni-300 steel, Phys. Procedia 12 (PART 1) (2011) 255–263, https://doi.org/10.1016/j.phpro.2011.03.033.
- [31] T. Bhardwaj, M. Shukla, Effect of laser scanning strategies on texture, physical and mechanical properties of laser sintered maraging steel, Mater. Sci. Eng. A 734 (June) (2018) 102–109, https://doi.org/10.1016/j.msea.2018.07.089.
- [32] S. Shakerin, A. Hadadzadeh, B.S. Amirkhiz, S. Shamsdini, J. Li, M. Mohammadi, Additive manufacturing of maraging steel-H13 bimetals using laser powder bed fusion technique, Addit. Manuf. 29 (January) (2019) 100797, https://doi.org/ 10.1016/j.addma.2019.100797.
- [33] F.F. Conde, et al., Effect of thermal cycling and aging stages on the microstructure and bending strength of a selective laser melted 300-grade maraging steel, Mater. Sci. Eng. A 758 (September 2018) (2019) 192–201, https://doi.org/10.1016/j. msea.2019.03.129.
- [34] T. Allam, K.G. Pradeep, P. Köhnen, A. Marshal, J.H. Schleifenbaum, C. Haase, Tailoring the nanostructure of laser powder bed fusion additively manufactured maraging steel, Addit. Manuf. 36 (September) (2020), https://doi.org/10.1016/j. addma 2020 101561
- [35] X. Xu, J. Ding, S. Ganguly, C. Diao, S. Williams, Oxide accumulation effects on wire + arc layer-by-layer additive manufacture process, J. Mater. Process. Technol. 252 (2018) 739–750. Feb. https://doi.org/10.1016/j.jmatprotec.2017.10.030.
- [36] F.F. Conde, J.A. Avila, J.P. Oliveira, N. Schell, M.F. Oliveira, J.D. Escobar, Effect of the as-built microstructure on the martensite to austenite transformation in a 18Ni maraging steel after laser-based powder bed fusion, Addit. Manuf. 46 (2021) 102122, https://doi.org/10.1016/j.addma.2021.102122.
- [37] F.F. Conde, J.D. Escobar, J.P. Oliveira, A.L. Jardini, W.W. Bose Filho, J.A. Avila, Austenite reversion kinetics and stability during tempering of an additively manufactured maraging 300 steel, Addit. Manuf. 29 (May) (2019) 100804, https:// doi.org/10.1016/i.addma.2019.100804.
- [38] B. Mooney, K.I. Kourousis, R. Raghavendra, Plastic anisotropy of additively manufactured maraging steel: influence of the build orientation and heat treatments, Addit. Manuf. 25 (October 2018) (2019) 19–31, https://doi.org/ 10.1016/j.addma.2018.10.032.
- [39] X. Xu, J. Ding, S. Ganguly, C. Diao, S. Williams, Preliminary investigation of building strategies of maraging steel bulk material using wire + arc additive manufacture, J. Mater. Eng. Perform. 28 (2) (2019) 594–600. Feb. https://doi. ore/10.1007/s11665-018-3521-5.
- [40] X. Xu, et al., Improving mechanical properties of wire plus arc additively manufactured maraging steel through plastic deformation enhanced aging response, Mater. Sci. Eng. A 747 (2019) 111–118. Feb. https://doi.org/10.1016/j. mseg. 2018.12.114
- [41] T. Debroy, S.A. David, Physical processes in fusion welding, Rev. Mod. Phys. 67 (1) (1995) 85–112, https://doi.org/10.1103/RevModPhys.67.85.
- [42] J.D. Escobar, et al., Meta-equilibrium transition microstructure for maximum austenite stability and minimum hardness in a Ti-stabilized supermartensitic stainless steel, Mater. Des. 156 (2018) 609–621, https://doi.org/10.1016/j. matdes.2018.07.018.
- [43] Ikpe Aniekan E., Owunna Ikechukwu, Ememobong Ikpe, Effects of arc voltage and welding current on the arc length of tungsten inert gas welding (TIG), Int. J. Eng. Technol. 3 (4) (2017) 213–221.
- [44] O. Dmitrieva, et al., Chemical gradients across phase boundaries between martensite and austenite in steel studied by atom probe tomography and

- simulation, Acta Mater. 59 (1) (2011) 364–374, https://doi.org/10.1016/j.
- [45] B. Rohit, N.R. Muktinutalapati, Austenite reversion in 18% Ni maraging steel and its weldments, Mater. Sci. Technol. (U. K.) 34 (3) (2018) 253–260, https://doi.org/ 10.1080/02670836.2017.1407544.
- [46] D. Raabe, D. Ponge, O. Dmitrieva, B. Sander, Nanoprecipitate-hardened 1.5 GPa steels with unexpected high ductility, Scr. Mater. 60 (12) (2009) 1141–1144, https://doi.org/10.1016/j.scriptamat.2009.02.062.
- [47] F. Niessen, T. Nyyssönen, A.A. Gazder, R. Hielscher, Parent grain reconstruction from partially or fully transformed microstructures in MTEX, J. Chem. Inf. Model. 53 (9) (2013) 1689–1699.
- [48] Z. Hu, X. Qin, T. Shao, H. Liu, Understanding and overcoming of abnormity at start and end of the weld bead in additive manufacturing with GMAW, Int. J. Adv. Manuf. Technol. 95 (5–8) (2018) 2357–2368, https://doi.org/10.1007/s00170-017-1392-9.
- [49] F. Montevecchi, G. Venturini, N. Grossi, A. Scippa, G. Campatelli, Idle time selection for wire-arc additive manufacturing: a finite element-based technique, Addit. Manuf. 21 (2018) 479–486. May, https://doi.org/10.1016/j.addma.2018.0 1.007.
- [50] H. Geng, J. Li, J. Xiong, X. Lin, Optimisation of interpass temperature and heat input for wire and arc additive manufacturing 5A06 aluminium alloy, Sci. Technol. Weld. Join. 22 (6) (2017) 472–483, https://doi.org/10.1080/ 13621718.2016.1259031.
- [51] P.F. Mendez, K.L. Niece, T.W. Eagar, Humping formation in high current GTA welding, in: International Conference on Joining of Advanced and Speciality Materials II, no. November, 1999, p. 8.
- [52] K.G. Prashanth, J. Eckert, Formation of metastable cellular microstructures in selective laser melted alloys, J. Alloys Compd. 707 (2017) 27–34, https://doi.org/ 10.1016/j.jallcom.2016.12.209.
- [53] R.A. Grange, C.R. Hribal, L.F. Porter, Hardness of tempered martensite in carbon and low-alloy steels, Metall. Trans. A. 8 A (11) (1977) 1775–1785, https://doi.org/ 10.1007/RPD046882
- [54] J.H. van der Merwe, G.J. Shiflet, The role of structural ledges at phase boundaries-III. F.C.C.-B.C.C. interfaces in Kurdjumov-Sachs orientation, Acta Metall. Mater. 42 (4) (1994) 1199–1205, https://doi.org/10.1016/0956-7151(94)90136-8.
- [55] C. Ranger, V. Tari, S. Farjami, M.J. Merwin, L. Germain, A. Rollett, Austenite reconstruction elucidates prior grain size dependence of toughness in a low alloy steel, Metall. Mater. Trans. A Phys. Metall. Mater. Sci. 49 (10) (2018) 4521–4535, https://doi.org/10.1007/s11661-018-4825-7.
- [56] T. Nyyssönen, M. Isakov, P. Peura, V.T. Kuokkala, Iterative determination of the orientation relationship between austenite and martensite from a large amount of

- grain pair misorientations, Metall. Mater. Trans. A Phys. Metall. Mater. Sci. 47 (6) (2016) 2587–2590, https://doi.org/10.1007/s11661-016-3462-2.
- [57] J. Hidalgo, M.J. Santofimia, Effect of prior austenite grain size refinement by thermal cycling on the microstructural features of as-quenched lath martensite, Metall. Mater. Trans. A Phys. Metall. Mater. Sci. 47 (11) (2016) 5288–5301, https://doi.org/10.1007/s11661-016-3525-4.
- [58] Y. Mine, K. Hirashita, H. Takashima, M. Matsuda, K. Takashima, Micro-tension behaviour of lath martensite structures of carbon steel, Mater. Sci. Eng. A 560 (2013) 535–544, https://doi.org/10.1016/j.msea.2012.09.099.
- [59] A.J. Kaijalainen, P.P. Suikkanen, T.J. Limnell, L.P. Karjalainen, J.I. Kömi, D. A. Porter, Effect of austenite grain structure on the strength and toughness of direct-quenched martensite, J. Alloys Compd. 577 (Suppl. 1) (2013) S642–S648, https://doi.org/10.1016/j.jallcom.2012.03.030.
- [60] S.C. Kennett, G. Krauss, K.O. Findley, Prior austenite grain size and tempering effects on the dislocation density of low-C Nb-Ti microalloyed lath martensite, Scr. Mater. 107 (2015) 123–126, https://doi.org/10.1016/j.scriptamat.2015.05.036.
- [61] C. Carson, Heat Treating of Maraging Steels, in: Heat Treating of Irons and Steels 4D, ASM International, 2014, p. 0. Oct. 01, 10.31399/asm.hb.v04d.a0005948.
- [62] J. Marcisz, J. Stępień, Short-time ageing of MS350 maraging steel with and without plastic deformation, Arch. Metall. Mater. 59 (2) (2014) 513–520, https://doi.org/ 10.2478/amm-2014-0085
- [63] J.M. Pardal, S.S.M. Tavares, V.F. Terra, M.R. Da Silva, D.R. Dos Santos, Modeling of precipitation hardening during the aging and overaging of 18Ni-co-Mo-Ti maraging 300 steel, J. Alloys Compd. 393 (1–2) (2005) 109–113, https://doi.org/ 10.1016/j.jallcom.2004.09.049.
- [64] K. Choo, et al., Heat retention modeling of large area additive manufacturing, Addit. Manuf. 28 (April) (2019) 325–332, https://doi.org/10.1016/j. addma.2019.04.014.
- [65] T.A. Rodrigues, V. Duarte, J.A. Avila, T.G. Santos, R.M. Miranda, J.P. Oliveira, Wire and arc additive manufacturing of HSLA steel: effect of thermal cycles on microstructure and mechanical properties, Addit. Manuf. 27 (2019) 440–450, https://doi.org/10.1016/j.addma.2019.03.029.
- [66] H. Nitta, et al., Diffusion of molybdenum in α-iron, Acta Mater. 50 (16) (2002) 4117–4125, https://doi.org/10.1016/S1359-6454(02)00229-X.
- [67] K. Nakazawa, Y. Kawabe, S. Muneki, Grain refinement of high-strength maraging steels through cyclic heat treatment, Mater. Sci. Eng. 33 (1) (1978) 49–56.
- [68] Z. Nasiri, S. Ghaemifar, M. Naghizadeh, H. Mirzadeh, Thermal mechanisms of grain refinement in steels: a review, Met. Mater. Int. (2020), https://doi.org/ 10.1007/s12540-020-00700-1. February.